Axial dispersion in curved channels in the presence of pulsating flow

Gleb Valitov[†], Damiano Rossi[†], Chris Price[‡], Asterios Gavriilidis[†], Luca Mazzei[†*]

[†] *University College London, Department of Chemical Engineering, Torrington Place, London WC1E 7JE, UK*

[‡] *EPSRC Centre for Innovative Manufacturing in Continuous Manufacturing and Crystallisation, University of Strathclyde, Technology and Innovation Centre, 99 George Street, Glasgow G1 1RD, U.K*

[*] *Corresponding author: l.mazzei@ucl.ac.uk*

Keywords: Coiled Flow Inverter, Helically Coiled Tube, Axial Dispersion, Residence Time Distribution, Microfluidics, Oscillatory Flow

Abstract

A narrow residence time distribution (RTD) is desirable in several chemical engineering processes. However, in systems operating at low Reynolds number, axial dispersion can be significant. To lower it, we utilized two mixing approaches: secondary flow achieved with curved geometries and oscillatory variation of the flow rate. We investigated their combined effect on axial dispersion in millifluidic channels with three geometries: straight tube, helically coiled tube (HCT) and coiled flow inverter (CFI). We studied the influence on axial dispersion of two key parameters of pulsating flows: amplitude and frequency of pulsation; in dimensionless form, these are expressed via the amplitude ratio and Strouhal number, respectively. For unsteady flow, we performed numerical simulations to characterise mixing. The results indicate that pulsation enhances radial mixing significantly. Our experimental studies show that axial dispersion is lower in the presence of pulsation, and increasing amplitude and/or frequency has a positive effect. For the same amplitude ratio and Strouhal number, axial dispersion decreases more in the CFIs than in the HCTs. Comparing two extremes, the straight capillary with steady flow (no RTD enhancement) and the CFI with pulsation (lowest axial dispersion achieved in our work), we observed a 10-fold reduction in the axial dispersion number.

1. Introduction

Micro and millifluidic devices tend to operate at low Reynolds number; this means that viscous forces dominate over inertial forces. The absence of turbulence implies that for the simplest devices (e.g., straight cylindrical channels) diffusion, a comparatively slow process, is the only mechanism of radial mixing. This limits mixing considerably. Therefore, significant research efforts into microfluidics focus on developing techniques that improve mass transfer. Mixing techniques can be *active* or *passive*. The first utilize external sources of energy to achieve better mixing; common examples are sound and ultrasound waves [1], including acoustic pressure fluctuations and bubble-induced vibrations, periodic flow rate variation [2] and the use of mechanical devices (for instance, small impellers [3] or integrated microvalves and pumps [4]). Passive mixing techniques utilize the flow energy to enhance mixing; they involve altering the geometry of the system (for instance, by adding baffles or mixing structures, or by curving the channel) to create eddies in the flow or decrease the diffusion path [5]. In this work, we combined active and passive mixing, using pulsation in curved capillaries.

In curved geometries (e.g., coils), Dean vortices form owing to centrifugal forces [6]. These vortices enhance radial mixing, and using them is a well-established passive mixing approach. The strength of Dean vortices is characterised by the Dean number, $\mathrm{Dn} \equiv \mathrm{Re}\sqrt{d/D_s}$, where D_s is the diameter of the support structure (which is twice the curvature radius), d is the diameter (or equivalent diameter) of the channel, and $\mathrm{Re} \equiv \rho u_b d/\mu$ is the Reynolds number, where u_b is the (time-independent) fluid mean velocity, while ρ and μ are the fluid density and dynamic viscosity, respectively.

Varying the flow rate periodically (a process called pulsation) is an active mixing approach established in the early 60s [7]; however, its potential is still being investigated by the flow chemistry community [8]. For oscillatory flows in curved channels, the time-dependent cross-sectional average axial velocity is equal to $u(t) = u_p \sin(2\pi f t) + u_b$, where t is the time, f is the pulsation frequency, and u_p is the amplitude of the sinusoidal part of the instantaneous fluid velocity. The oscillatory Dean and Reynolds numbers can be defined as $\mathrm{Dn_o} \equiv \mathrm{Re_o}\sqrt{d/D_s}$ and $\mathrm{Re_o} \equiv (\alpha + 1)\,\mathrm{Re}$, respectively, where $\alpha \equiv u_p/u_b$ is the amplitude ratio. Note that in the literature different definitions exist for the oscillatory Reynolds number; this dimensionless group is defined in terms of either u_p or of $u_p + u_b$. In this work, we based the definition on $u_p + u_b$ (the resulting Reynolds number is sometimes referred to as total Reynolds number). In these flows, another key dimensionless quantity is the Strouhal number, $\mathrm{St} \equiv fd/u_b$. St can be regarded as a dimensionless frequency. In the literature, researchers have used $\mathrm{Re_o}$, $\mathrm{Dn_o}$, α and St to characterize the effects of pulsation on Dean flows, but in the present work we opted for the equivalent set Re, Dn, α and St. Using the dimensionless numbers α and Re is convenient, because it allows decoupling the periodic part of the flow from the bulk part of the flow.

The simplest curved structure is the helically coiled tube (HCT), a tube wrapped around a cylindrical support, where the centrifugal force acting on the fluid generates two symmetrical Dean vortices. However, this simple structure presents two dead zones at the centre of each vortex, where the radial velocity is zero; moreover, the convective mixing between the two vortices is limited. To overcome these limitations, Saxena and Nigam [9] proposed coiled flow inverters (CFIs), where 90^o bends are introduced in the support structure to change the direction of the centrifugal force and in turn of the Dean vortices. Owing to the absence of mixing dead zones, CFIs enhance mixing more than HCTs. The residence time distribution (RTD) for both systems has been extensively studied at steady state [10-14]; these studies showed that HCTs reduce the axial dispersion when compared to straight tubes, but CFIs reduce it even more [9-11, 12, 14].

Dispersion in pulsating flows was first investigated by Aris [7], who solved the problem analytically and showed that pulsation increases the axial dispersion coefficient slightly, its effect rarely contributing a fraction of more than 1/128 to the total dispersion coefficient. However, his work concerned straight tubes and laminar flows. Further research has shown that pulsation can generate turbulence and, at sufficiently high frequency and amplitude, turbulence reduces dispersion [15-17].

In curved geometries, if the pulsation amplitude is sufficiently high, Lyne instabilities arise [18]. These shift the Dean vortices to the outer walls and form two additional vortices in the centre of the tube [19]. Sudo et al. [20] established that Lyne instabilities appear solely for $\alpha > 19$, but they also reported that for flows at lower amplitude ratio (in the range 6-10), deformed Dean vortices are present ~~[20]~~. The effects of both Lyne instabilities and Dean vortices have been investigated for HCTs; Pedley and Kamm reported that for flows where Re and Dn are constant, axial dispersion decreases with an increase in frequency when $\beta^2 \equiv fd^2/4k > 10$, where k is the tracer diffusivity [21]. Recently, there have been advances on this topic, with McDonough et al [22] highlighting the benefits of using HCTs in operating conditions just before the onset of Lyne instabilities. This work showed that axial dispersion can be reduced with an increase in either the Strouhal number or the amplitude ratio.

Other works have investigated pulsation in straight channels with baffles. An entire set of reactors, referred to as continuous oscillatory baffled reactors (COBRs), was developed for these applications. Despite significant geometrical differences between HCTs/CFIs and COBRs, one can draw a parallel between Dean vortices and vortices formed around baffles, because both form owing to the channel geometry. It has been established that in COBRs nearly plug-flow behaviour can be achieved either at high flow rates or at lower flow rates in the presence of pulsation, the latter offering the additional benefit of longer space-time [23]. Moreover, for different configurations of baffles, it was observed that the width of the RTD reduces when the amplitude ratio increases [24–26]. Mazubert et al. [27]

compared the performance of COBRs and helical reactors in the presence of pulsation, showing that these two systems offer similar benefits.

This work investigates experimentally and numerically the behaviour of straight tubes, HCTs and CFIs in the presence of pulsation. The main motivation is achieving a narrow RTD while maintaining the desired space-time (L/u_b, where L is the length of the tube), thus keeping the bulk flow rate constant. As said, two dimensionless groups were selected to characterize flow pulsation: amplitude ratio (α) and Strouhal number (St). The other dimensionless groups characterising the flow (e.g., Re, Dn and L/d) were kept constant to maintain a constant space-time in the selected geometry. Large values of the amplitude ratio permitted investigating the operational region where turbulence starts occurring and the interaction between the latter and Dean vortices. At the same time, we aimed to maintain both Strouhal number and amplitude ratio low enough to prevent the formation of Lyne instabilities, focussing on operating conditions that have received limited attention in the literature. This paper is organised as follows. Section 2 presents the experimental procedure and the method employed to implement pulsation. In Section 3, we investigate straight and curved tubes via numerical simulations, the results revealing the effects of Strouhal number and amplitude ratio on radial mixing. Finally, in Section 4, we present the experimental investigation of the effects of pulsation on axial dispersion in straights tubes, HCTs and CFIs.

2. Experimental methodology

The schematic of the experimental setup used for residence time distribution measurements is shown in Figure 1. 100 ml glass syringes (SGE Analytical Science) were filled with carrier fluid (deionized water) and tracer fluid (75 mg/L solution of Basic Blue 3, Dye content 25%, Sigma-Aldrich, diffusivity in water $D_m = 6.4 \cdot 10^{-10}\ \mathrm{m}^2/\mathrm{s}$). With a syringe pump (Harvard Apparatus PHD 2000), these fluids were simultaneously pumped to a six-way injection HPLC valve (M-461, IDEX) that allowed switching between carrier fluid and tracer fluid to flow within the tube, thereby enabling a step change in concentration of blue dye at the tube inlet. Before the experiment, the carrier fluid was pumped through the system. At the start of the experiment, the feed was changed to tracer fluid. An additional syringe pump (KDS Scientific Legato 210) with a 5 ml glass syringe (SGE Analytical Science) filled with heptane ($H_3C(CH_2)_5CH_3$, >97% pure, VHR) was connected with a T-junction (PEEK, 0.5 mm thru-hole, IDEX Health & Science) to the main tube via a short polytetrafluoroethylene (PTFE) tube (~10 cm length, 1 mm I.D., 1.6 mm O.D., Bohlender). The main tubes were also from PTFE and were ~5 m long, with 1 mm I.D. and 1.6 mm O.D. Their exact length varied by 5-10 cm and was measured for each HCT and CFI. Each support structure for both HCTs and CFIs had a diameter D_s of 17 mm, and there were 8 turns on each of 10 arms of the CFI. There were 90 ± 1 turns in total for each HCT (depending on the exact length of the tube). All connector tubes were also made of PTFE.

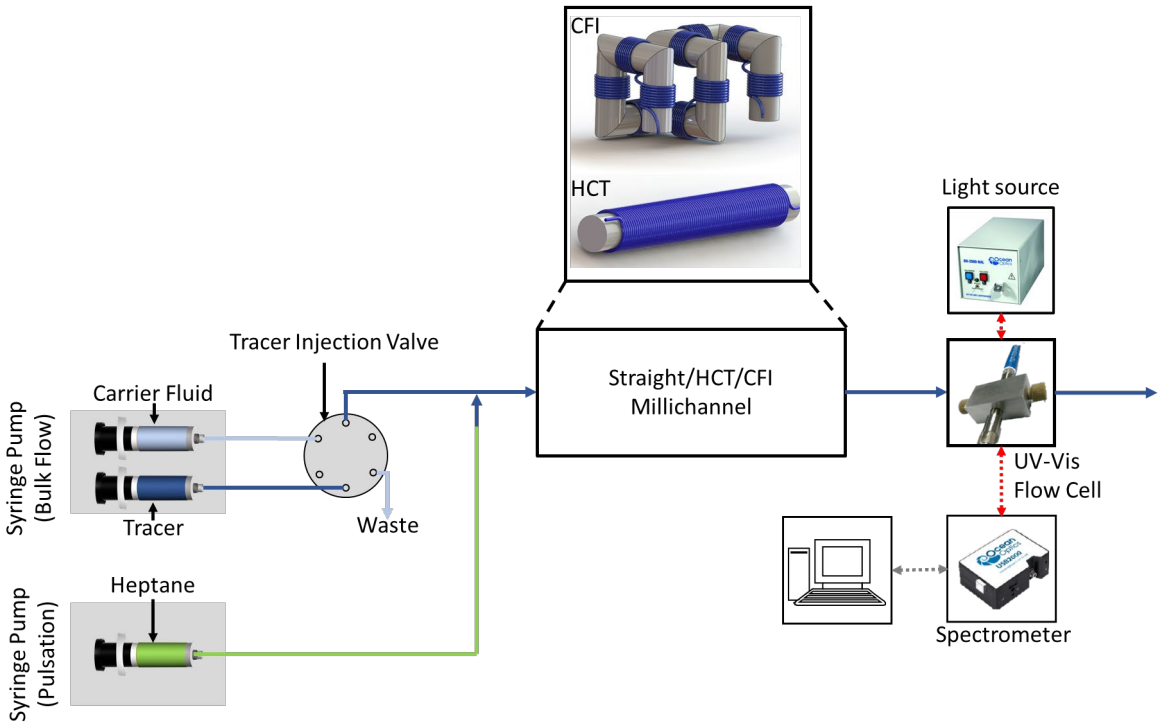

Figure 1: Schematic representation of the residence time distribution measurement system with a UV-Vis detection flow cell.

When pulsation is applied during the experiments, the tracer may diffuse back from the T-junction towards the pulsation syringe pump. Documented in the literature [2], this issue has been observed if the capillary tube between the pulsation syringe pump and the main tube is filled with carrier fluid. To avoid this problem, inside this capillary tube we employed heptane. Since blue dye and water are insoluble in heptane, the heptane/water interface behaves like a piston, allowing pulsating the flow while preventing the tracer from diffusing back into the pulsation syringe. Moreover, utilizing heptane allows reducing the dead zone in the capillary tube between the pulsation syringe pump and the main tube; the length of this dead zone was only 1 cm and can be considered to be negligible in comparison to the 5 m length of the main tube. Before each RTD experiment, we ensured that the experimental system operated at pseudo-steady-state (i.e. same behaviour during each pulsation cycle). The tracer was not injected until all the heptane droplets and air bubbles had left the system and no additional heptane droplets were forming (the interface between heptane and water became stable). To pulsate the flow, on the pulsation syringe pump we switched periodically between the *infuse* and *withdrawal* functions. The net bulk flow (characterized by the time-independent velocity u_b) was delivered via the bulk-flow syringe pump, which was operated at constant flow rate. The combination of the two flows resulted in the pulsatile flow through the channel. The distance between the HPLC valve and the T-

junction where the pulsating pump and bulk flow combined, did not exceed 5 cm, which is negligible in comparison to the 5 m length of the main tube. In the pulsation syringe pump, we could set three quantities: flow rate amplitude (related to u_p), pulsation period (related to f) and displaced volume of liquid in the syringe; only two had to be specified to define the operation of the pump. For this study, we changed a) the flow rate amplitude to vary the amplitude ratio and b) the period of pulsation to vary the frequency (or equivalently the Strouhal number). This is the only way to vary α and St independently of each other. The values of the parameters studied in this work are given in Table 1.

Bulk velocity	u_b	$0.021\ \mathrm{m/s}$
Amplitude of the sinusoidal part of the velocity	u_p	$0.021 - 0.21\ \mathrm{m/s}$
Length of the (main) tube	L	$5\ \mathrm{m}$
Inner tube diameter	d	$0.001\ \mathrm{m}$
Support structure diameter	D_s	$0.017\ \mathrm{m}$
Coil-to-tube ratio	d/D_s	0.059
Dean number	$\mathrm{Dn} \equiv \mathrm{Re}\sqrt{d/D_s}$	5.1
Reynolds number	$\mathrm{Re} \equiv \rho u_b d/\mu$	21.2
Concentration of the tracer	$-$	$75\ \mathrm{mg/L}$
Amplitude ratio	$\alpha \equiv u_p/u_b$	$0 - 10$
Frequency	f	$0.1 - 2\ \mathrm{Hz}$
Strouhal number	$\mathrm{St} \equiv fd/u_b$	$0.0047 - 0.094$
Oscillatory Reynolds number	$\mathrm{Re}_o \equiv (\alpha + 1)\ \mathrm{Re}$	$21.2 - 212$
Oscillatory Dean number	$\mathrm{Dn}_o \equiv \mathrm{Re}_o\sqrt{d/D_s}$	$5.1 - 51$

Table 1: Values of the parameters studied in this work.

The tracer concentration was measured at the tube outlet via UV-Vis spectroscopy. As discussed in our previous work [11], the light absorption was directly proportional to the concentration according to the Beer-Lambert law for the range of dye concentration used in this study. A light source (Ocean Optics DH-2000-BAL) was connected via a fibre optic cable to one side of a flow cell through which the main tube passed. The other side of the flow cell was connected, via another fibre optic cable, to a spectrophotometer (Ocean Optics USB2000+ UV–Vis-ES), where the light intensity was measured at regular intervals of 0.1 s. The average light intensity in the 645-660 nm wavelength region (which

corresponds to the wavelength of light absorbed by the blue dye) was recorded by the Ocean Optics Spectra Suite software. Before each experiment, the light absorption of tube wall and pure water were measured and removed as background. Then, the collected absorbance data were postprocessed: the detector noise was removed via a Savitzky-Golay filter, and the resulting data were converted from absorbance to concentration using the linear relationship between them.

The measured outlet concentration, $\mathrm{C(t)}$, was converted into a cumulative distribution function, $\mathrm{F(t)}$, by normalising the curve. The RTD function, $\mathrm{E(t)}$, was then calculated by differentiating $\mathrm{F(t)}$ with respect to time. To simplify the process, we calculated $\mathrm{E(t)}$ by normalizing and differentiating the absorbance curve (because the Beer-Lambert law applies and the normalized absorbance is equivalent to the normalized concentration). Thus, $\mathrm{E(t)}$ was calculated as follows:

$$\mathrm{E(t)} = \frac{1}{A_{\max}} \frac{\mathrm{dA(t)}}{\mathrm{dt}} \qquad (1)$$

where A is the absorbance and $A_{\max}$ is its maximum value (achieved at the concentration of tracer of 75 mg/L). To compare experimental results more easily, we made $\mathrm{E(t)}$ dimensionless:

$$\mathrm{E_\theta(\theta)} \equiv \tau\, \mathrm{E(t)} \qquad (2)$$

where $\theta \equiv t/\tau$ is the dimensionless time and $\tau \equiv L/u_b$ is the space-time.

In the literature, dimensionless axial dispersion numbers ($\mathrm{N_d}$ or $\mathrm{N_L}$) are often used to characterise hydrodynamic dispersion within a system (these are defined by Eq. 3). These dimensionless numbers can be calculated from the experimental results by fitting the predictions of the axial dispersion model (ADM), described by Eqs. 4 and 5, to the experimental data [28]. The fitting was done using MATLAB Curve Fitting Toolbox via the least square method, where $\mathrm{D_{ax}}$ was the fitting parameter. The residual error did not exceed 10^{-3}. Based on $\mathrm{D_{ax}}$, calculated from the fitting, the corresponding values of $\mathrm{N_d}$ and $\mathrm{N_L}$ were determined using Eq. 3. The exact length and internal diameter of the tube were measured for each structure for accurate ADM fitting. The diameter was determined by measuring experimentally the volume of the entire tube and then calculating the mean diameter. The length of the tube was kept at 5 ± 0.2 m, and the internal diameter was 1 ± 0.03 mm. The measured values were used during the ADM fitting. The system had open-open boundaries, and we took care to operate in the region where the ADM holds. For straight tubes, this region is identified in the flow map reported in Rossi et al. [11], with the Bodenstein number ($u_b d/D_m$, where D_m is the tracer diffusivity) and the tube length-to-diameter ratio (L/d) as coordinates. In our work, these were equal to $3 \cdot 10^4$ and $4 \cdot 10^4$, respectively. Under these conditions, the flow falls in the region of the map where the ADM holds. Moreover, the ADM should be applicable in HCTs and CFIs when the residual error of the fitting does not exceed 10^{-3} [11], which is the case for all the experiments conducted in our work.

$$\mathrm{N_d} \equiv \frac{D_{ax}}{u_b\, d};\quad \mathrm{N_L} \equiv \frac{D_{ax}}{u_b\, L} \tag{3}$$

$$E_{ADM} = \frac{1}{\sqrt{4\pi D_{ax} t}} \exp\left[-\frac{(L - u_b\, t)^2}{4D_{ax} t}\right] \quad \text{for } \mathrm{N_L} > 0.01 \tag{4}$$

$$E_{ADM} = \sqrt{\frac{{u_b}^3}{4\pi D_{ax} L}}\, exp\left[-\frac{(L - u_b\, t)^2}{4D_{ax} L/u_b}\right] \text{ for } \mathrm{N_L} < 0.01 \tag{5}$$

Above, D_{ax} is the axial dispersion coefficient, u_b is the time-independent mean fluid velocity, d is the internal diameter of the tube and L is the length of the tube. Note that N_L is the inverse of the vessel Peclet number.

Initially, in order to characterise the pulsation generated by the pump, the flow rate was measured. The flow rate values were obtained by injecting a small air bubble into the tube between the pulsation pump and the main channel, measuring the time-dependent displacement of the centre of the bubble, and determining the bubble velocity. The bubble diameter was equal to the tube diameter. Assuming that the slip between the fluid and the bubble is negligible, the bubble velocity is equal to the mean fluid velocity, which is directly proportional to the flow rate. The measurements were conducted by taking repeat images (at constant frame rate) and using image processing to identify how much the bubble had moved. The measurements were taken three times per second, and the results were smoothed using a 3-point moving average. The results are reported in Figure 2. The sinusoidal wave was generated using the pump settings (specifying the flow rate amplitude and frequency). The flow rate of the pulsation pump closely resembles a sinusoidal wave; thus, for the numerical modelling of the system, we assumed a sinusoidal pulsating flow rate profile.

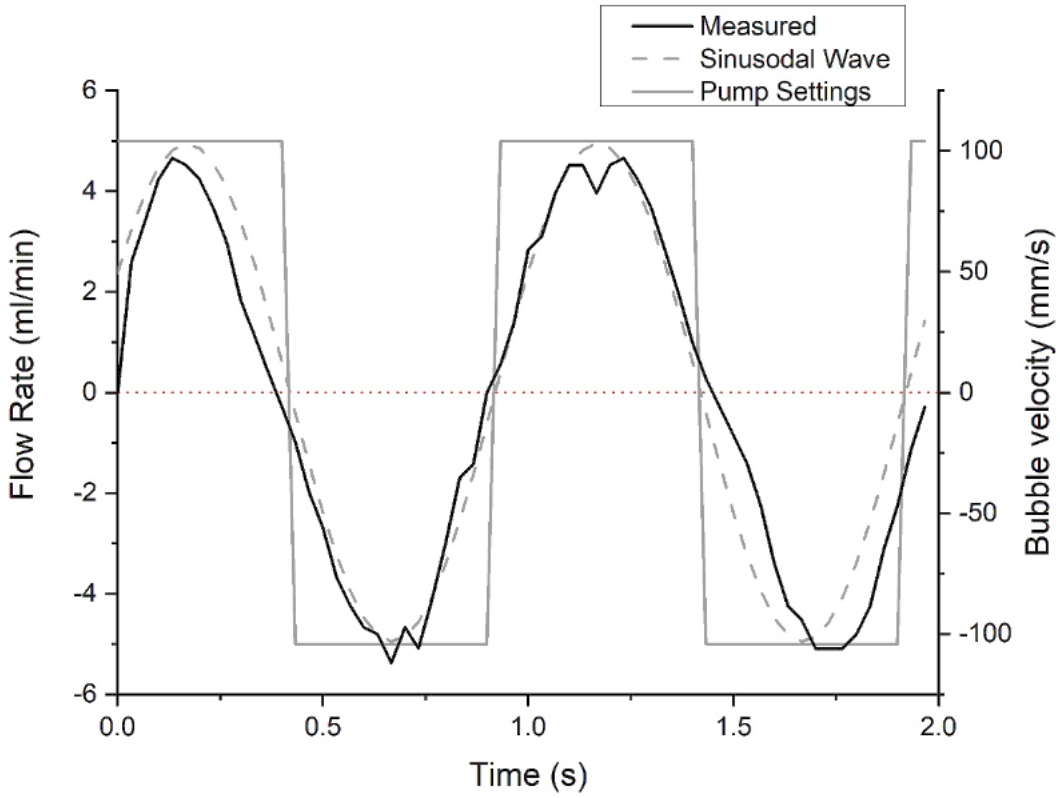

Figure 2: Flow rate delivered by the pulsation pump at a pulsation frequency of 1 Hz. Black solid line: experimentally measured bubble velocity and corresponding flow rate; grey dashed line: sinusoidal wave; grey solid line: flow rate (and corresponding bubble velocity) specified with the pump settings. The periodic flow rate produced by the pulsation syringe pump closely resembles a sinusoidal wave.

3. Numerical simulation of hydrodynamics in HCTs

The work reported in this section involves the numerical simulation of the flow in a 4-turn helically coiled tube (HCT) for one full cycle of pulsation. Literature findings show that, for steady-state flows, Dean vortices fully develop within the first turn, which acts as an upstream development region [29]. Our numerical results confirmed this; however, to be conservative, we considered the first two turns as development region. We modelled the pulsating flow at the highest amplitude ratio used in the experiments, where the length of the development region is expected to be the longest. For $\mathrm{Dn} < 7$ and $\alpha < 10$, our simulations showed that, at all times during one period of pulsation, the velocity field remains the same in the turns after the second one; therefore, we assumed that the velocity field in the third turn of the HCT was representative of all the other subsequent 84 turns (two turns constitute the development region near the inlet and the outlet of the capillary). Hence, we used the numerical simulation of the first four turns of the structure to assess the behaviour of the entire structure. For the CFI, a similar approach could not be used, because the introduction of 90° turns in the support

structure prevented us from extrapolating the behaviour of the first few turns to the subsequent ones. The entire CFI structure must be simulated, a task that is too demanding computationally. For this reason, we investigated CFIs only experimentally.

The three-dimensional velocity profile was computed (using COMSOL Multiphysics 5.3) by solving the Navier-Stokes and continuity equations:

$$\rho\frac{\partial \mathbf{u}}{\partial \mathrm{t}} + \rho(\mathbf{u}\cdot\nabla\mathbf{u}) - \mu\nabla^2\mathbf{u} + \nabla \mathrm{P} = 0 \qquad (6)$$

$$\nabla\cdot\mathbf{u} = 0 \qquad (7)$$

where $\mathbf{u}$ and P denote the velocity and dynamic pressure of the fluid, respectively. Eqs. 6 and 7 were integrated numerically for a specified geometry in transient conditions. Pure water was used as fluid for all simulations. No-slip boundary conditions at the wall were set ($\mathbf{u} = \mathbf{0}$ at $r = R$, where r is the radial coordinate and R is the radius of the tube). At the tube outlet, a Dirichlet boundary condition for pressure was set. Since we are only interested in the change in pressure, the value for the pressure was set to 0. The resultant boundary condition reads $P = 0$ at $x = L$, where x is the axial coordinate. At the tube inlet, a normal inflow velocity boundary condition was used, where the velocity magnitude varied with time ($u_{in} = u_p \sin(2\pi f t) + u_b$ at $x = 0$, where t is the time). Note that the parabolic velocity profile develops within the first quarter of a turn, and so using a laminar velocity profile or a uniform velocity profile as boundary condition at the tube inlet does not affect the simulation results. To improve numerical convergence, initially the flow field simulation was conducted at steady state in the absence of pulsation. The solution to this simulation was then used as the initial condition for the time-dependent simulations of pulsating flow. The total volume of the 4-turn structure was 470 mm^3 and was divided in 628483 mesh elements; further refinement of the mesh did not change the results appreciably (for details, refer to the Supplementary Information). The simulations were performed on a PC with Intel Xeon E5 3.5 GHz CPU and 192 GB of RAM. The computational time step was kept at least three orders of magnitude lower than the period of pulsation. The total computed time for each simulation was at least two pulsation periods. The results are displayed on a cutting plane normal to the tube to show the radial velocity field; which cutting plane is used is unimportant (for all the radial velocity profiles are the same), as long as it is after the second turn.

The results show the presence of Dean vortices within the tube, as can be observed in Figure 3a. These results agree with the literature [30,31], where similar flow patterns were observed in fully developed Dean vortices. A shift of the axial velocity peak is also observed (Figure 3b), a fact that is known and has been reported in the literature [e.g., 6]. The legend in Figure 3a shows the magnitude of the component of the velocity vector parallel to the cross-section of the tube; this is significantly smaller

than the magnitude of the axial velocity component. For example, while the magnitude of the peak axial velocity is 4.07 cm/s, the maximum magnitude of the radial velocity component (owing to the Dean vortices) is 0.16 cm/s. It might appear that the convective mass transport induced by Dean vortices is negligible, but this is not the case. When comparing straight tubes to HCTs, one must contrast the diffusion time in the radial direction for the former with the convection time in the radial direction for the latter, because these phenomena are responsible for radial mixing in the corresponding systems. These characteristic times are given by:

$$\mathrm{t}_{\text{radial diffusion}} \sim \frac{d^2}{D_m} \tag{8}$$

$$\mathrm{t}_{\text{radial convection}} \sim \frac{d}{u_D} \tag{9}$$

where d is the diameter of the tube, u_D is the velocity scale within the Dean vortices, and D_m is the molecular diffusion coefficient. The velocity within the Dean vortices varies in the tube cross-section, as can be observed in Figure 3a. In Eq. 9, the velocity scale can be taken to be the maximum velocity within the Dean vortices. The cross-section mean velocity can be used as well, since these values are within one order of magnitude of each other. The radial diffusion time (for $D_m = 6.4 \cdot 10^{-10}\ \mathrm{m^2/s}$ and $d = 1\ \mathrm{mm}$) was ~1500 s, while the radial convection time (based on the maximum velocity within the Dean vortices) was ~0.6 s. Hence, in the presence of centrifugal forces, radial mixing improves significantly, while axial dispersion reduces significantly. So, the width of the RTD in the HCT should be smaller than that in the straight tube, as reported in the literature [9, 11, 14].

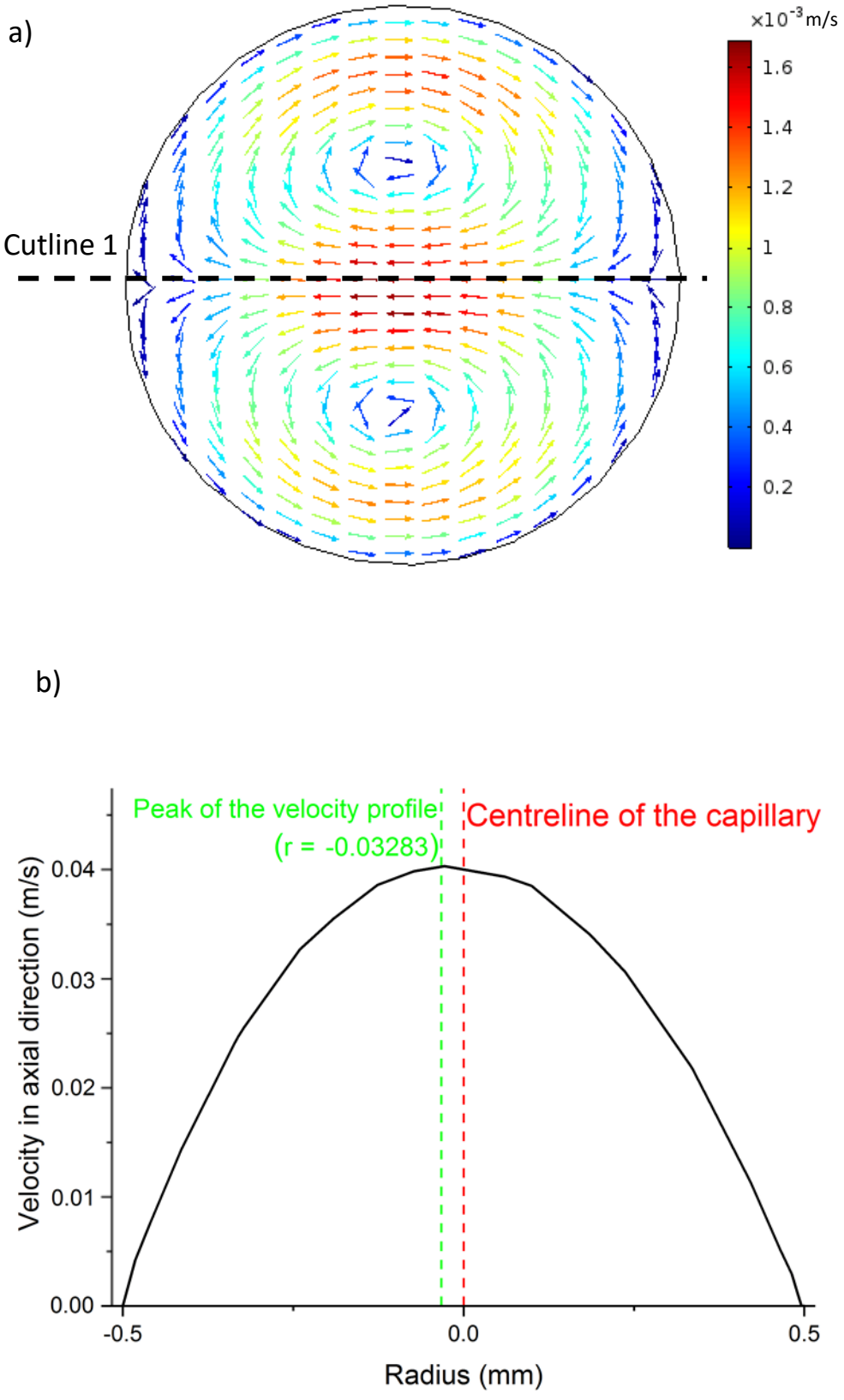

Figure 3: (a) Velocity field over a cross-section of the helically coiled tube after two turns without pulsation. The colour legend represents the velocity magnitude. (b) Axial velocity profile along Cutline 1. The mean axial velocity is 2.12 cm/s.

For simulations with pulsation, the mean (i.e., cross-sectional averaged) axial velocity was taken to be sinusoidal, as shown in Figure 2. The velocity becomes negative around the trough of the pulsation cycle, because for amplitude ratios greater than one, the maximum flow rate of the pulsating flow (Au_p) is larger than the flow rate of the main flow (Au_b). In the presence of pulsation, the maximum value of the mean axial velocity is time-dependent (this value, however, is uniform along the axis on the tube). The highest magnitude of this cross-sectional averaged axial velocity is at the peak of the pulsation cycle. At the trough of the cycle, the absolute value of the mean axial velocity is lower than that at the peak, but is higher than its time-averaged value (u_b, the bulk velocity). In fact, for most of the cycle the absolute value of the mean axial velocity is higher than the mean axial velocity of a steady-state process with the same space-time (please, refer to the Supplementary Information for further discussion). The radial velocity due to Dean vortices increases with the increase in the mean axial velocity of the fluid. This is seen in Figure 4, where the radial velocity over one pulsation period is displayed for $\mathrm{St} = 0.044$ (for equivalent axial velocities and our comments on axial flow patterns refer to the Supplementary Information). We performed similar simulations over a range of Strouhal numbers (varying the pulsation frequency); for each simulation, we calculated the radial convection time for the pulsating flow, using Eq. 9. In this equation, to find the velocity scale u_D, we operated as follows. At each time t, we extracted from the simulation the maximum value of the radial velocity of the fluid; these velocities were then averaged over one pulsation period as follows:

$$u_D = f \int_0^{1/f} |\mathrm{u}_{\mathrm{rad.\ max}}(\mathrm{t})|\ \mathrm{dt} \qquad (10)$$

So, the velocity scale u_D coincides with the time-averaged maximum radial velocity. This approach is only applicable when the period of pulsation is at least an order of magnitude smaller than the space-time; this was the case for all our results, the difference being 2-3 orders of magnitude.

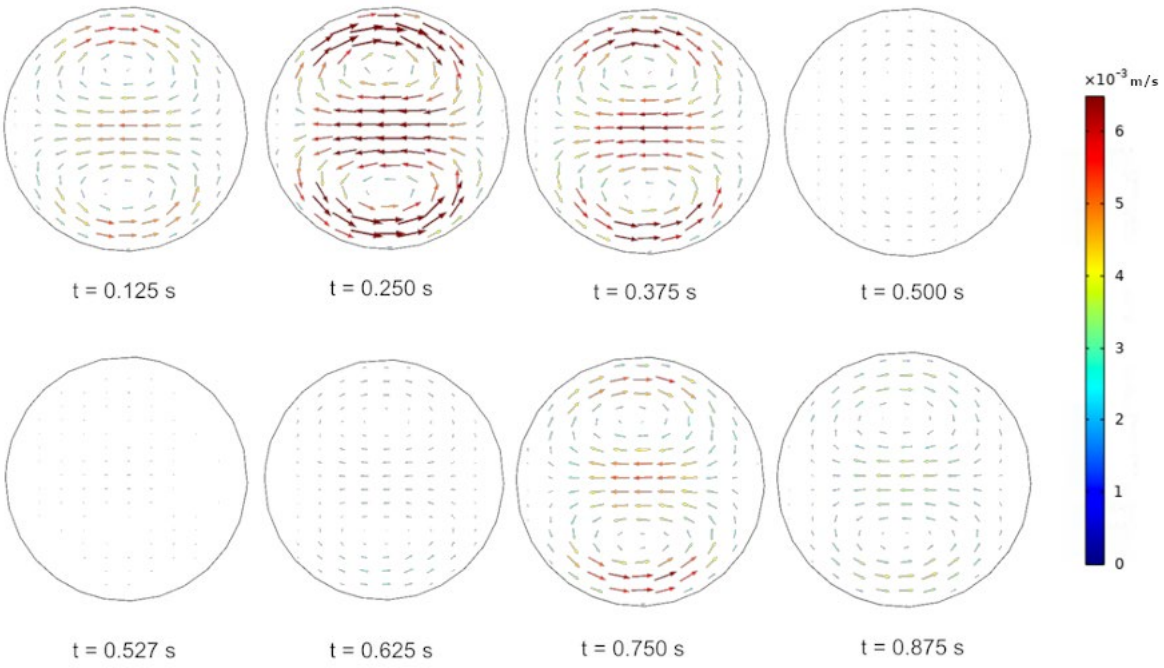

Figure 4: Radial velocity field inside a curved tube during one period of pulsation (P = 1 s). Re = 21, Dn = 5, α = 10, St = 0.044. At t = 0.527 s, the axial velocity averaged over the cross-section of the tube is zero, because the flow direction changes.

Based on the above approach, we calculated the radial convection time as a function of the Strouhal number and amplitude ratio. The results are shown in Figures 5 and 6, where the radial convection time is normalized by the characteristic diffusion time (see Eq. 8). This ratio yields the inverse of the Peclet number, but the velocity scale used here is that of the radial velocity, not of the entire velocity vector. Figure 5 shows the variation of the dimensionless radial convection time with the Strouhal number. We observe that, within the range of conditions studied in this work, the dimensionless radial convection time is independent of the frequency of pulsation (the small variations observed in the graph are due to numerical discretization). However, at all Strouhal numbers, the radial convection time was four times lower than that in the non-pulsating flow (corresponding to $\mathrm{St} = 0$). So, one would expect axial dispersion to be lower in the presence of pulsation.

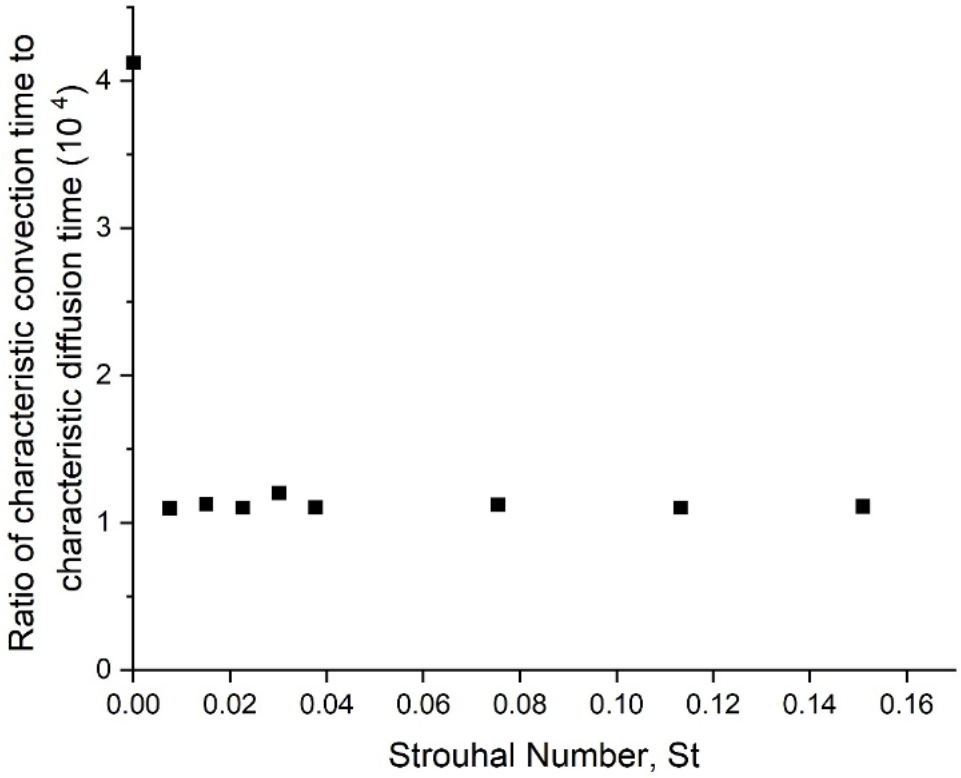

Figure 5: Dimensionless time-averaged radial convection time for pulsating flow in a curved tube as a function of the Strouhal Number for Re = 21, Dn = 5, α = 10. The data point at St = 0 corresponds to non-pulsating flow.

A similar behaviour was observed when the amplitude of pulsation was varied (which is represented in dimensionless form by the amplitude ratio). The results are displayed in Figure 6. In this case, the dimensionless radial convection time gradually decreases with the amplitude ratio. When α increases, the mean axial velocity and in turn the mean radial velocity increase, so that the radial convection time decreases (while the diffusion time remains constant). In addition, a higher pulsation amplitude ratio results in a smaller fraction of time where the absolute value of the inlet velocity is lower than the bulk velocity. Both effects lead to a decrease in the radial convection time, justifying the trend observed in Figure 6.

The numerical results reveal that radial mixing is more vigorous in the presence of pulsation. For the conditions investigated, the frequency of pulsation should have no effect on the radial mixing caused by Dean vortices and similar RTDs should be observed at all frequencies. By contrast, the amplitude of pulsation affects significantly the radial velocity, and we would expect to observe narrower RTDs at higher amplitudes.

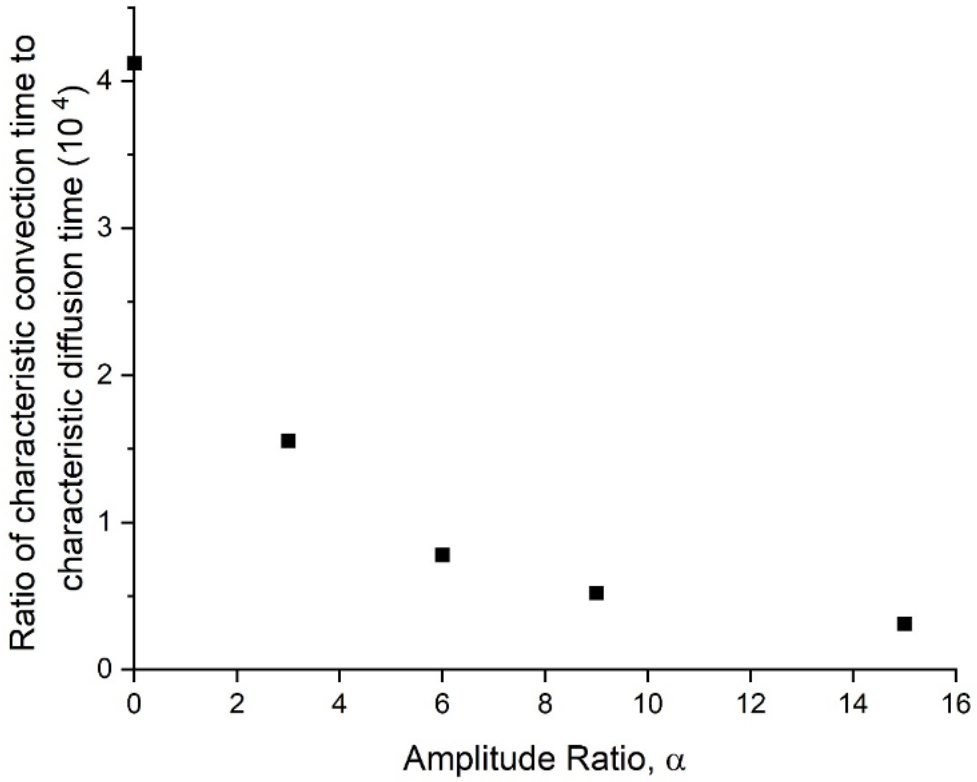

Figure 6: Dimensionless time-averaged radial convection time for pulsating flow in a curved tube as a function of the amplitude ratio for Re = 21, Dn = 5, St = 0.025. The data point at α = 0 corresponds to non-pulsating flow.

One more observation must be made. In all the presented cases and at all the operating conditions described in Section 3, fully-formed Dean vortices were observed and the effect of Lyne instabilities was insignificant. Research conducted in a tube with I.D. of 14.1 mm [20] suggests that the deformation of Dean vortices (due to the onset of Lyne instabilities) should start at amplitude ratios above 6. However, this is not the case for the smaller tubes used in our work, where viscous forces are much higher. Thus, in our system the onset of Lyne instabilities should occur at higher amplitude ratios [20]. We did not observe Lyne instabilities at amplitude ratios less than 12, but at higher amplitudes, slight deformation of Dean vortices is expected to occur, and at amplitude ratios higher than 15, we did see such flow patterns in our numerical simulations.

4. Experimental results on RTD in straight tubes, HCTs and CFIs

We investigated the RTD for curved geometries in the presence of pulsation experimentally. We fitted each measured RTD to the axial dispersion model (ADM) [28], obtaining the resulting axial dispersion number as outlined in Section 2. We considered three geometries: straight tube, helically coiled tube (HCT) and coil flow inverter (CFI). Sample RTD curves for one of the experiments are shown in Figure 7. The periodic fluctuations observed in Figure 7(a) are due to the pulsation of the flow; these fluctuations are absent in Figure 7(b), because the curve was smoothed.

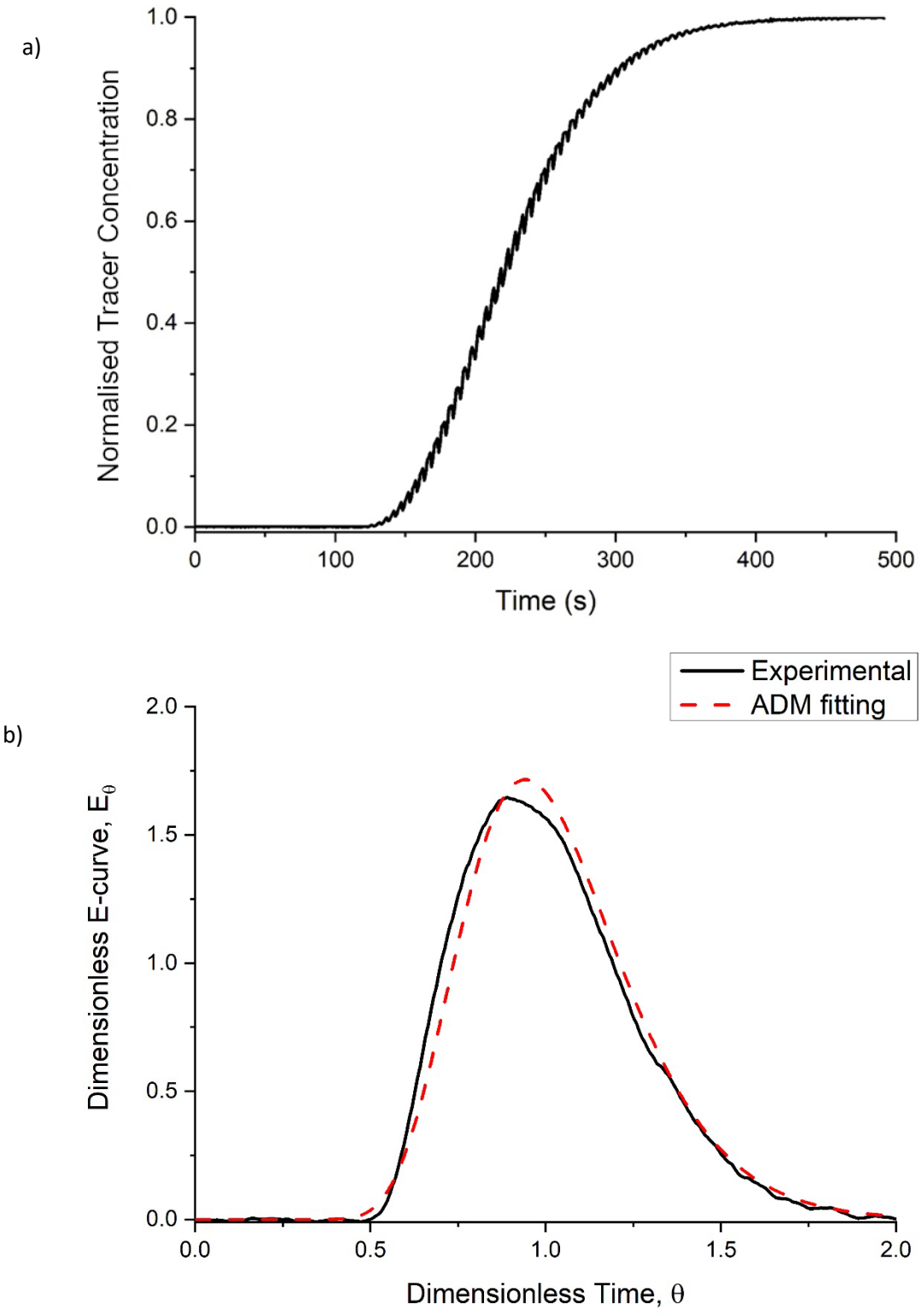

Figure 7: Experimental results from RTD experiments at Re = 21, Dn = 5, α = 10, St = 0.044 in an HCT. (a) Unprocessed F-curve showing the variation of the normalised tracer concentration with time. (b) E-curve after noise removal, smoothing, nondimensionalization and ADM fitting. The relative error of fitting did not exceed 10^{-3}.

When comparing the performance of the three systems for a fixed amplitude ratio, we noticed (Figure 8) that the CFI and HCT perform similarly in the presence of pulsation, while both present lower axial

dispersion than the straight tube. In the absence of pulsation, the CFI performing better than the HCT is well-established in the literature [9,11] and is due to the presence of 90° bends in the CFI, which vary the direction of the Dean vortices and remove the mixing dead zones existing in the HCT.

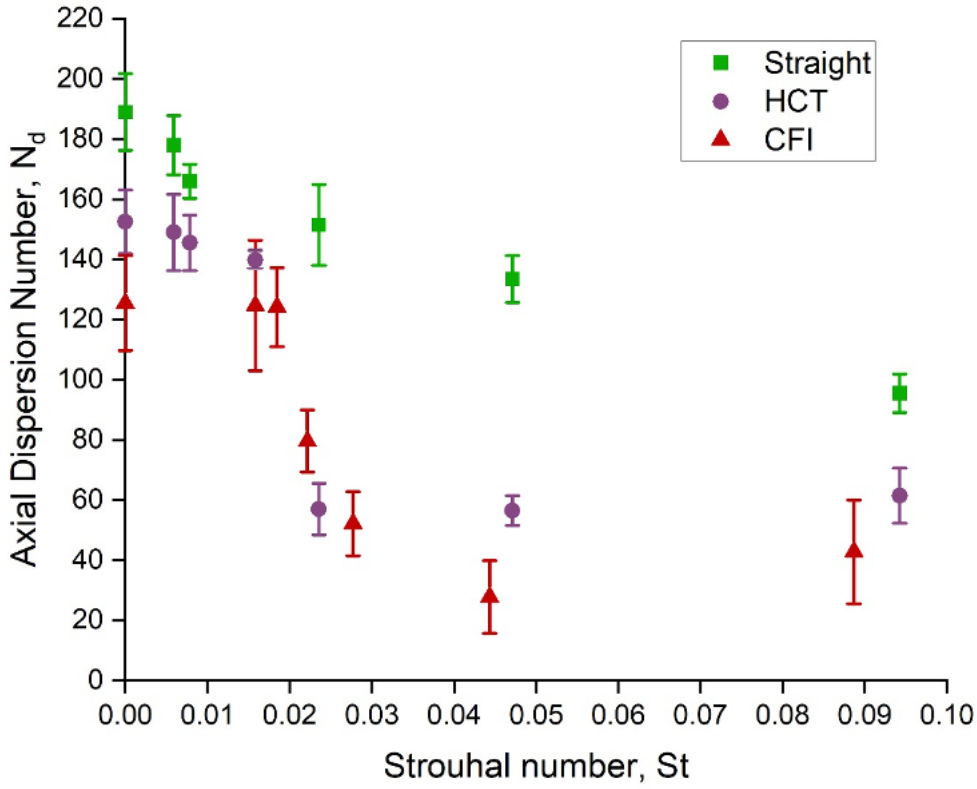

Figure 8: Axial dispersion number as a function of the Strouhal number for Re = 21, Dn = 5, α = 10 for the three tubes (straight, HCT, CFI). The data points at St = 0 correspond to non-pulsating flow.

For the straight tube, the decrease in axial dispersion coefficient with the Strouhal number might be unexpected, since, for laminar flow, pulsation should increase axial dispersion, even if by a very small amount [7]. However, this is not necessarily the case at high amplitude ratios and frequencies, since the flow may not be laminar. In pulsating flows, the transition from the laminar to the turbulent regime occurs at far lower values of Re than in steady-state flows [32,33]. For example, the flow of a fluid oscillating around a point with no net flow can be turbulent if the amplitude ratio or frequency are sufficiently high, even if $\mathrm{Re} = 0$. Various studies have determined the critical oscillatory Reynolds number (Re_o) at which the flow becomes turbulent [34,35]; however, these values are system specific. Ahn and Ibrahim [17] developed an empirical correlation, expressed in terms of a Reynolds number based on the Stokes-layer thickness:

$$\sqrt{2}\,\mathrm{Re}_{\delta,\mathrm{critical}} = (211)^{\frac{8}{7}}\left(\sqrt{\mathrm{Va}}\right)^{\frac{1}{7}} \quad (10)$$

$$\mathrm{Re}_{\delta} \equiv \rho\, u_{max}\, \delta/\mu \quad ; \quad \mathrm{Va} \equiv \pi\rho f d^2/\, 2\mu \quad (11)$$

$$\delta = \, (2\mu/\rho f)^{0.5} \quad (12)$$

$$u_{max} \equiv (\alpha + 1)u_b \equiv u_b + u_p \quad (13)$$

Here Va is the Valensi number, u_{max} is the maximum magnitude of the cross-sectional mean velocity during one pulsation cycle, and δ is the Stokes-layer thickness (a parameter used to describe periodic flows around no-slip boundaries). Turbulence is present if Re_{δ} exceeds its critical value, given by Eq. 10. Based on this equation, for the present system, the critical value of Re_{δ} is in the range of 280-300. In our experiments, Re_{δ} is in the range of 20-450, suggesting that turbulence may occur in our system. Note that this correlation indicates a *developed* turbulent flow; weak turbulence is reported to occur at lower values of Re_{δ} [34]. For example, a study has reported temporary turbulence during a change of flow direction at $\mathrm{Re}_{\delta} = 200$ [36]. The onset of turbulence in pulsating flows is still being actively investigated, and the scientific community still has to agree on when it is expected to occur. Various investigations have determined the critical Reynolds number at which the transition from laminar to turbulent flow should occur [34,35], but these findings are not detailed enough to yield reliable values of the critical Reynolds number for the systems considered in our work.

A correlation for an exact value of the onset of weak turbulence is unavailable in the literature. We could try to employ CFD to understand if turbulence is expected to occur in the experiments described in this work. Standard turbulence models $k-\varepsilon$, $k-\omega$ or their combination do not provide sufficient accuracy to evaluate the turbulence caused by pulsation, an issue discussed in depth in the literature [17]. There have been several advances in the field of modelling the transitional regime for pulsating flow, such as the model developed by Lovik et at. [37] or the three equation $k-k_L-\omega$ model, which describes intermittent turbulent fluctuations during pulsating flows [38]. Developing or implementing an accurate CFD model to understand eddy formation is beyond the scope of this study and, despite recent advances, the models available are insufficient to fully describe the behaviour of our systems.

Several other literature sources have considered the dispersion in pulsating flows in straight tubes. At high St, the flow tends to develop turbulent regions that reduce dispersion [38]. Our results for straight tubes are in agreement with experimental [40] and theoretical [15] findings in the literature, where, when the frequency is increased (at sufficiently high amplitude ratios), a rapid fall in axial dispersion is reported. Another literature source presents a reduction in the axial dispersion number when α/St exceeds 20-30 [36]. The onset of turbulence is the key mechanism for the reduction of axial dispersion in straight tubes, and based on literature findings, onset of turbulence or intermittent turbulence are

expected in the system we considered. This highlights the importance of conducting experiments in straight tubes for comparison with curved geometries, since intermittent turbulence is hard to identify from numerical methods [37, 38], while experiments (in combination with prior literature findings) may suggest its existence.

In curved geometries, pulsation reduces axial dispersion more significantly than in straight tubes. In the HCT, when the Strouhal number increases, the axial dispersion number decreases. For St<0.02, the reduction is modest, less than 10%. For 0.02<St<0.03, the effects of pulsation are significant and dispersion reduces appreciably. For St>0.03, the dispersion number plateaus, which indicates that the maximum possible reduction in axial dispersion has been reached. In HCTs, radial mixing occurs owing to Dean vortices and, as discussed in the numerical section, a change in frequency has limited effect on them (the radial convection time does not vary significantly when the frequency increases). In light of this, one could expect a negligible dependence of $\mathrm{N_d}$ on St. However, between and at the centres of the Dean vortices, convective mixing is essentially absent and, as a result, mixing dead zones exist, with no mixing across the centreline of the tube. In non-oscillatory HCTs, this issue is solved by utilizing CFIs, where varying the direction of the centrifugal force changes the direction of the Dean vortices, thereby eliminating mixing dead zones. In oscillatory HTCs, oscillations can lead to a similar outcome, inducing mixing between and within the Dean vortices through the temporary turbulence that occurs when the direction of the flow changes. As the pulsation frequency (i.e. St) increases, the flow changes direction more frequently, and this justifies the reduction in axial dispersion observed in Figure 8 for 0.02<St<0.03.

In the CFI, a similar trend to the HCT is observed. For St<0.02, there is no reduction in dispersion, or, if a reduction is present, this is of the order of magnitude of the error bars. At St>0.02, $\mathrm{N_d}$ reduces rapidly and eventually plateaus at a value in the range 20-50, which is similar to that found for the HCT (50-60). As discussed above, the main benefit of CFIs over HCTs is the elimination of the mixing dead zones owing to the change in direction of the Dean vortices. In the presence of pulsation, turbulence has a similar effect, so the benefits of using the CFI instead of the HCT are reduced.

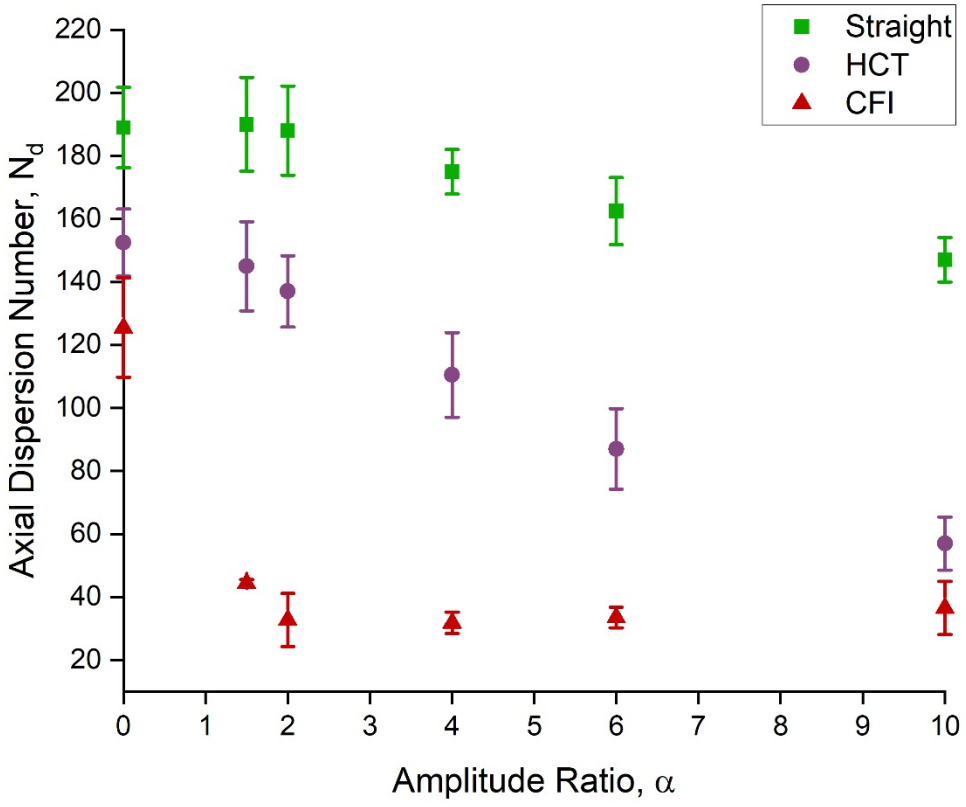

Figure 9: Axial dispersion number as a function of the amplitude ratio for Re = 21, Dn = 5, St = 0.044 for the three tubes (straight, HCT, CFI). Not all error bars are visible; some error bars are in the order of magnitude of the marker. The data points at α = 0 correspond to the non-pulsating flow.

The results of the experiments where the amplitude ratio (α) was altered are shown in Figure 9. In the straight tube and the HCT, the axial dispersion number decreases with the amplitude ratio, while in the CFI it first decreases and then plateaus. For a straight tube, pulsation reduces axial dispersion owing to the onset of turbulence, as discussed above. Pulsation affects axial dispersion more significantly in curved geometries. This further indicates that pulsation enhances the Dean vortices. In the HCT, experiments show that increasing the amplitude ratio makes the axial dispersion number gradually decrease, while the numerical results (Figure 6) indicate that an increase in amplitude ratio makes radial mixing gradually more vigorous, thus decreasing the radial convection time. There is no established empirical correlation between radial convection time and axial dispersion number, but we expect that axial dispersion should decrease when radial mixing becomes more vigorous; this indicates that the numerical and experimental results agree. In the CFI, the introduction of pulsation leads to a significant, and more abrupt, decrease in the axial dispersion number, from 123 to 29. This reduction is fully achieved at $\alpha = 2$, and a further increase in amplitude ratio has little effect on axial dispersion. In the CFI, for both Strouhal number and amplitude ratio, the dispersion number plateaus; this plateau

indicates the highest reduction in axial dispersion that one may achieve (in the systems investigated) by combining the effects of pulsation and Dean flow.

Pulsation can affect temporary turbulence in two ways. As said above, temporary turbulence primarily occurs when the flow changes direction. An increase in amplitude ratio or Strouhal number both lead to an increase in the rate of variation of the flow rate at its inversion point, and this increases the turbulence *intensity*. But increasing the Strouhal number also leads to an increase in the *frequency* at which the change in flow direction occurs, and so to an increase in the frequency of turbulent events. The significant difference in the values of the axial dispersion number between the HCT and the CFI in Figure 9 suggests that, within the operating conditions considered, an increase in the amplitude ratio (increase only in the intensity of temporary turbulence, but not in the frequency of its events) does not eliminate the mixing dead zones, since the variations in the direction of the Dean vortices in the CFI leads to a further significant reduction in dispersion. By contrast, the small difference in the $\mathrm{N_d}$ values between the HCT and the CFI in Figure 8 suggests that an increase in the Strouhal number (increase in both the frequency of turbulent events and their intensity) essentially eliminates the mixing dead zones, because in this case the variations in the direction of the Dean vortices in the CFI do not result into a further significant reduction in dispersion. This analysis shows that the reduction in axial dispersion owing to temporary turbulence is primarily guided by the frequency of the turbulent events, and therefore by the frequency at which the direction of the flow changes.

An increase in amplitude ratio has other beneficial effects; in particular, it increases the velocity within the Dean vortices, which leads to stronger radial mixing. Thus, in Figure 9, for the HCT $\mathrm{N_d}$ decreases with α for two reasons: as α increases, the intensity of temporary turbulence and the velocity within the Dean vortices increase. Both effects reduce dispersion, and the second is likely dominant. In this case, temporary turbulence does not eliminate the mixing dead zones and so $\mathrm{N_d}$ does not plateau. In Figure 9, for the CFI, $\mathrm{N_d}$ decreases with α for the same two reasons, but here also the variation in the direction of the Dean vortices contributes to reducing $\mathrm{N_d}$. This contribution plays a key role, as it allows $\mathrm{N_d}$ to plateau, suggesting that in this case the mixing dead zones are eliminated.

When the issues of the mixing dead zones has been addressed and the velocity of the Dean vortices is high enough, we obtain the maximum possible reduction in dispersion, as indicated by $\mathrm{N_d}$ plateauing at high St and amplitude ratio. This plateau can only be achieved when a mechanism for eliminating the mixing dead zones is present. In Figure 8, for the HCT, this mechanism is the rise in the frequency of temporary turbulence events, which occurs due to the rise in frequency of flow inversion events. In Figure 9, for the CFI, this mechanism is due to the change in the direction of the Dean vortices, while in Figure 8, again for the CFI, both of the above mechanisms act together.

Literature findings for studies in millifluidic HCTs at high oscillatory Dean (in the range of 70-200) and Reynolds numbers (in the range of 10-50) also suggest a decrease in axial dispersion with increase in amplitude ratio and Strouhal number until a maximum possible reduction is achieved; further increase in amplitude ratio and Strouhal number have the opposite effect [22]. In our work, we found that when the amplitude ratio varies, a configuration change from HCT to CFI is shown to have a more significant effect on the reduction of axial dispersion than going from a straight capillary to an HCT. This difference is most substantial for amplitude ratios in the range 1-4, a range that can be reasonably achieved in milliscale channels. One can avoid using the CFI by operating at higher amplitude ratios in the HCT, but this comes at the cost of higher pressure drop and pumping requirements, especially in channels at the border between milliscale and microscale (d<1mm).

Finally, one can draw a parallel between a continuous oscillating baffle reactor (COBR) and curved tubes. Slavnic [24] developed a correlation for the axial dispersion number (referred to as reciprocal of the Peclet number) based on the Reynolds number, Strouhal number and amplitude ratio. This correlation, based on experimental data by the author as well as by others in the literature [41–44], suggests that the axial dispersion number for a COBR operated at similar conditions (amplitude ratio and Strouhal number) to our system is in the region of 30-50. Thus, as we can see from Figures 8 and 9, our millifluidic CFI performs similarly to a COBR. While in the HCT the efficiency of mixing is lower, a low axial dispersion number can still be achieved at high Strouhal number and/or amplitude ratio. Ahmed et al. [25] showed that a COBR operated in similar conditions to those discussed in this work behaves similarly, axial dispersion decreasing with the amplitude ratio (up to $\alpha < 10$). In general, the CFI and HCT operated with pulsation match the performance of an equivalent COBR in terms of mixing, while simplicity of manufacturing adds additional appeal.

5. Conclusions

This work aimed to investigate axial dispersion in curved tubes in the presence of a pulsating flow. We developed an experimental system to conduct RTD experiments, imposing a step change in tracer concentration at the tube inlet and measuring the tracer concentration via UV-Vis spectroscopy at the tube outlet. Experiments without pulsation were also conducted for comparison. We studied the effects of two key parameters: amplitude ratio and Strouhal number. The results indicated that pulsation leads to narrower RTDs, the effect being more pronounced at higher amplitude and frequency of pulsation. The axial dispersion number in the coiled flow inverter with pulsation can be an order of magnitude lower than that in a straight tube without pulsation (the maximum variation being from 190 to 20). Using the coiled flow inverter and pulsation independently reduced the axial dispersion number from 190 to 120 and 100, respectively. Numerical simulations supported the experimental results, showing that in the presence of pulsation the characteristic radial mixing time

reduces considerably. The difference between numerical simulations and experimental results, along with literature findings, suggests the existence of temporary turbulence caused by pulsation. There are two key factors that affect the axial dispersion in helically coiled tubes: a) existence of mixing dead zones between and within Dean vortices and b) low radial velocity within the Dean vortices. The first factor is addressed by using more complex structures, such as coiled flow inverters, or by introducing oscillatory flows with sufficiently high frequency, which can generate turbulence. The second factor is addressed by increasing the instantaneous axial velocity magnitude; this can be achieved by increasing the amplitude of the oscillatory flow. When both factors are addressed, the maximum reduction (for the systems considered) in axial dispersion can be achieved. When this happens, the value of the axial dispersion coefficient plateaus. The results show a promising technique for reducing the RTD width and attaining a performance similar to that of continuous oscillatory baffled reactors, with systems that are easier and cheaper to manufacture.

Acknowledgments

Financial support for this work through an Innovation Grant from the Centre of Nature Inspired Engineering (EPSRC Grant EP/K038656/1) is gratefully acknowledged.

Bibliography

[1] Z. Yang, S. Matsumoto, H. Goto, M. Matsumoto, R. Maeda, Ultrasonic micromixer for microfluidic systems, Sens. Actuators, A. 93 (2001) 266–272.

[2] I. Glasgow, N. Aubry, Enhancement of microfluidic mixing using time pulsing, Lab Chip. 3 (2003) 114–120.

[3] L.-H. Lu, K.S. Ryu, C. Liu, A magnetic microstirrer and array for microfluidic mixing, J. Microelectromech Syst. 11 (2002) 462–469.

[4] J. Voldman, M.L. Gray, M.A. Schmidt, Liquid mixing studies with an integrated mixer/valve, in: D.J. Harrison et al. (eds.) Micro Total Analysis Systems, Springer Netherlands, Dordrecht, (1998) 181–184.

[5] V. Hessel, H. Löwe, F. Schönfeld, Micromixers - A review on passive and active mixing principles, Chem. Eng. Sci. 60 (2005) 2479–2501.

[6] W.R. Dean, Note on the motion of fluid in a curved pipe, Philos. Mag. 4 (1928) 673–695.

[7] R. Aris, On the dispersion of a solute in pulsating flow through a tube, Proc. R. Soc. A Math. Phys. Eng. Sci. 259 (1960) 370–376.

[8] P. Bianchi, J.D. Williams, C.O. Kappe, Oscillatory flow reactors for synthetic chemistry applications. J. Flow Chem., 10 (2020) 475-490.

[9] A.K. Saxena, K.D.P. Nigam, Coiled configuration for flow inversion and its effect on residence time distribution. AIChE J., 30 (1984) 363-368.

[10] F.S.P. Rojahn, V. Hessel, K.D.P. Nigam, F. Schael, Applicability of the axial dispersion model to coiled flow inverters containing single liquid phase and segmented liquid-liquid flows, Chem. Eng. Sci. 182 (2018) 77-92.

[11] D. Rossi, L. Gargiulo, G. Valitov, A. Gavriilidis, L. Mazzei, Experimental characterization of axial dispersion in coiled flow inverters, Chem. Eng. Res. Des. 120 (2017) 159–170.

[12] C. Castelain, A. Mokrani, P. Legentilhomme, H. Peerhossaini, Residence time distribution in twisted pipe flows: Helically coiled system and chaotic system, Exp. Fluids. 22 (1997) 359–368.

[13] T. Koray Palazoglu, K.P. Sandeep, Effect of holding tube configuration on the residence time distribution of multiple particles in helical tube flow, J. Food Process Eng. 25:4 (2002) 337–350.

[14] L. Sharma, K.D.P. Nigam, S. Roy, Single phase mixing in coiled tubes and coiled flow inverters in different flow regimes, Chem. Eng. Sci. 160 (2017) 227–235.

[15] E.J. Watson, Diffusion in oscillatory pipe flow, J. Fluid Mech. 133 (1983) 233–244.

[16] P. Joshi, K.D.P. Nigam, E.B. Nauman, The Kenics static mixer: new data and proposed correlations, Chem. Eng. J. Biochem. Eng. J. 59:3 (1995) 265–271.

[17] K.H. Ahn, M.B. Ibrahim, Laminar/turbulent oscillating flow in circular pipes, Int. J. Heat Fluid Flow. 13:4 (1992) 340–346.

[18] W.H. Lyne, Unsteady viscous flow in a curved pipe, J. Fluid Mech. 45 (1971) 13–31.

[19] B. Timité, C. Castelain, H. Peerhossaini, Mass transfer and mixing by pulsatile three-dimensional chaotic flow in alternating curved pipes, Int. J. Heat Mass Transf. 54 (2011)

3933–3950.

[20] K. Sudo, M. Sumida, R. Yamane, Secondary motion of fully developed oscillatory flow in a curved pipe, J. Fluid Mech. 237 (1992) 189–208.

[21] T.J. Pedley, R.D. Kamm, The effect of secondary motion on axial transport in oscillatory tube flow, J. Fluid Mech. 193 (1988) 347–367.

[22] J.R. McDonough, S. Murta, R. Law, A.P. Harvey, Oscillatory fluid motion unlocks plug flow operation in helical tube reactors at lower Reynolds numbers (Re ≤ 10), Chem. Eng. J. 358 (2019) 643–657.

[23] B.O. Olayiwola, G. Schaldach, P. Walzel, Residence time distribution of steady and pulsed flow in a parallel-plate channel with staggered fins, Chem. Eng. Technol. 34 (2011) 937–945.

[24] D.S. Slavnić, L.V. Živković, A.V. Bjelić, B.M. Bugarski, N.M. Nikačević, Residence time distribution and Peclet number correlation for continuous oscillatory flow reactors, J. Chem. Technol. Biotechnol. 92:8 (2017) 2178–2188.

[25] S.M.R. Ahmed, A.N. Phan, A.P. Harvey, Scale-up of oscillatory helical baffled reactors based on residence time distribution, Chem. Eng. Technol. 40:5 (2017) 907–914.

[26] R. Kacker, S.I. Regensburg, H.J.M. Kramer, Residence time distribution of dispersed liquid and solid phase in a continuous oscillatory flow baffled crystallizer, Chem. Eng. J. 317 (2017) 413–423.

[27] A. Mazubert, M. Crockatt, M. Poux, J. Aubin, C. Roelands, Reactor comparison for the esterification of fatty acids from waste cooking oil, Chem. Eng. Technol. 38 (2015) 2161–2169.

[28] O. Levenspiel, Chemical reaction engineering, 3rd ed., John Wiley & Sons, New York, (1999).

[29] B. Mujawar, M. Raja Roa, Flow of non-newtonian fluids through helical coils, Ind. Eng. Chem. Process Des. Dev. 17:1 (1978) 22–27.

[30] R.L. Manlapaz, S.W. Churchill, Fully developed laminar convection from a helical coil,

Chem. Eng. Commun. 9 (1981) 185–200.

[31] C.G. Slominski, W.D. Seider, S.W. Churchill, J.D. Seader, Helical and lemniscate tubular reactors, Ind. Eng. Chem. Res. 50:15 (2011) 8842–8850.

[32] D. Hershey, C.S. Im, Critical reynolds number for sinusoidal flow of water in rigid tubes, AIChE J. 14:5 (1968) 807–809.

[33] T. Sarpkaya, Experimental determination of the critical Reynolds number for pulsating Poiseuille flow, J. Basic Eng. 88:3 (1966) 589–598.

[34] M. Hino, M. Sawamoto, S. Takasu, Experiments on transition to turbulence in an oscillatory pipe flow, J. Fluid Mech. 75 (1976) 193–207.

[35] M. Ohmi, M. Iguchi, I. Urahata, Flow patterns and frictional losses in an oscillating pipe flow, JSME 25 (1982) 536–543.

[36] Song, J., Law, A.W. Longitudinal dispersion of turbulent oscillatory pipe flows. Environ Fluid Mech 15 (2015) 563–593.

[37] R. D. Lovik, J. P. Abraham, W. J. Minkowycz & E. M. Sparrow, Laminarization and turbulentization in a pulsatile pipe flow, Numerical Heat Transfer, Numer. Heat Transf.; A: Appl., 56:11 (2009), 861–879.

[38] A. Ramadan, A. El-Rahman, A. Sabry. Assessment of the transition $k - k_L - \omega$ model application to transitional oscillatory pipe flows, J. Acoust. Soc. Am.. 145 (2019) 1195–1204

[39] V. Levenspiel, O. Smith, Notes on the diffusion-type model for longitudinal mixing of fluids in flow, Chem. Eng. Sci. 8 (1957) 227–287.

[40] C.H. Joshi, R.D. Kamm, J.M. Drazen, A.S. Slutsky, An experimental study of gas exchange in laminar oscillatory flow, J. Fluid Mech. 133 (1983) 245–254.

[41] A.W. Dickens, M.R. Mackley, H.R. Williams, Experimental residence time distribution measurements for unsteady flow in baffled tubes, Chem. Eng. Sci. 44:7 (1989) 1471–1479.

[42] M.R. Mackley, X. Ni, Experimental fluid dispersion measurements in periodic baffled

tube arrays, Chem. Eng. Sci. 48:18 (1993) 3293–3305.

[43] M.R. Mackley, X. Ni, Mixing and dispersion in a baffled tube for steady laminar and pulsatile flow, Chem. Eng. Sci. 46:12 (1991) 3139–3151.

[44] W.M. Rohsenow, J.P. Hartnett, E.N. Ganic, Handbook of heat transfer fundamentals, 2nd ed., McGraw-Hill Book Co., New York, (1985).